Solvation of Carbon Nanotubes in a Room-Temperature Ionic Liquid

Youngseon Shim[†] and Hyung J. Kim[†,‡,*]

[†]Department of Chemistry, Carnegie Mellon University, Pittsburgh, Pennsylvania 15213, and [‡]School of Computational Sciences, Korea Institute for Advanced Study, Seoul 130-722, Korea

ABSTRACT Single- and double-walled carbon nanotubes in the armchair configuration solvated in the room-temperature ionic liquid 1-ethyl-3-methylimidazolium tetrafluoroborate ($EMI^+BF_4^-$) are studied *via* molecular dynamics (MD) computer simulations. Cations and anions show smeared-out, cylindrical shell-like distributions outside of the nanotubes irrespective of the nanotube diameter. The ion distributions inside the nanotubes vary markedly with their diameter. For example, in the case of (*n*,*n*) single-walled nanotubes, EMI^+ and BF_4^- ions separately form single-shell zigzag and chiral distributions for (8,8) and (10,10), respectively, while (12,12) develops a second internal solvation structure. The first internal solvation shell of (15,15) nanotubes consists of alternating layers of cations and anions along the nanotube axis. In the azimuthal direction, these cations and anions, respectively, form a pentagonal structure, whereas the corresponding ions for (20,20) show disordered octagonal structures. The smallest nanotube that allows solvent ions inside the tunnel is (7,7) with a diameter of 0.95 nm, which shows a single file distribution of internal ions. Imidazole rings of cations in the first internal and external solvation shells are mainly parallel to the nanotube surface, indicating π-stacking between the nanotubes and EMI^+ ions there.

KEYWORDS: solvation · ionic liquid · imidazolium ion · carbon nanotube · bucky gels · micropore · molecular dynamics simulations

Room-temperature ionic liquids (RTILs) based on bulky and asymmetric organic cations have received intensive scrutiny recently.[1−3] RTILs, usually liquid at or near room temperature, are nonvolatile, nonflammable, and thermally stable. As such, they provide an environmentally benign "green" alternative to organic solvents for chemical synthesis,[4−6] extractions,[7−10] and biocatalysis.[11,12] Due to their high intrinsic conductivity and wide electrochemical window as well as nonvolatility, RTILs are also an excellent candidate for an electrolyte in electrochemical devices such as batteries,[13,14] fuel cells,[15,16] and dye-sensitized solar cells.[17−19]

Recently, Aida and co-workers[20,21] found that RTILs are capable of dispersing carbon nanotubes. Specifically, when a powder of ground single-walled carbon nanotubes (SWNTs) was mixed with an excess amount of imidazolium-based RTILs, gelatinous materials ("bucky gels") were formed, which can be processed into different shapes without disrupting nanotube structures. The formation of bucky gels is not limited to SWNTs or imidazolium-based ionic liquids. Since the original work in ref 20, several groups have found that similar gelation is obtained for a variety of different carbon nanotubes and RTILs.[22−27] Because of the unique properties of bucky gels arising from their composite nature, *viz.*, nonvolatility and thermal stability of RTILs and high electronic conductivity of nanotubes, their potential application in fabrication of new soft materials and in electrochemical devices is of wide scope.

Properties of RTILs confined in the interior of carbon nanotubes have also been studied.[28] X-ray diffraction results seem to indicate that 1-butyl-3-methylimidazolium hexafluorophosphate ($BMI^+PF_6^-$) forms a crystal structure in the inside of nanotubes. According to differential scanning calorimetry measurements, the crystal thus formed is considerably more stable with a higher melting point than bulk $BMI^+PF_6^-$.

Despite rapidly growing interest in composite systems of carbon nanotubes and RTILs, they are not well-understood at the molecular level. There has been virtually no systematic study of these systems with simulation methods. Even efforts to understand, for example, solvation of benzene-like molecules[29−31] and graphite surfaces[32] in RTILs, which have some bearing, albeit remote, on nanotube−RTIL composite systems, have been quite limited to the best of our knowledge. As an initial attempt to gain theoretical understanding of these composite systems, we study solvation of small carbon nanotubes in $EMI^+BF_4^-$ *via* MD simulations.

*Address correspondence to hjkim@cmu.edu.

Received for review February 25, 2009 and accepted June 25, 2009.

Published online July 7, 2009.
10.1021/nn900195b CCC: $40.75

In this article, we analyze the structure of $EMI^+BF_4^-$ inside and outside of single- and double-walled nanotubes in the (*n*,*n*) armchair configuration. Seven different SWNTs (*i.e.*, $n = 6$, 7, 8, 10, 12, 15, and 20) are examined. For double-walled nanotubes (DWNTs), we consider two commensurate cases, (10,10)/(15,15) and (15,15)/(20,20), where the first and second chiral vectors of a pair (*n*,*m*)/(*n*′,*m*′) describe the configurations of the inner and outer nanotubes of a DWNT, respectively. In the simulations, both ends of the nanotubes were terminated with hydrogen atoms with the Lennard-Jones parameters $\varepsilon = 15.2$ K and $\sigma = 242$ pm and partial charge $+0.1e$. This charge assignment is roughly based on DFT results of ref 33. The C−H bond length employed for the termination is 109 pm. The carbon atoms directly bonded to the terminal H atoms have a partial charge of $-0.1e$, while all others are assumed to be electrically neutral. The Lennard-Jones parameters employed for C atoms of the nanotubes are $\varepsilon = 43.2$ K and $\sigma = 340$ pm.[34] For EMI^+ and BF_4^-, the flexible all-atom potential model of refs 35 and 36 was used. During the simulations, the nanotubes were held rigid with carbon bond length $l_{CC} = 141.5$ pm[37] and nanotube length $h = 3.742$ nm, defined as the end-to-end, hydrogen-to-hydrogen distance. MD results were obtained by computing averages from a 12 ns production run in the canonical ensemble at $T = 350$ K.

RESULTS AND DISCUSSION

We begin with RTIL densities inside SWNTs and their variations with the size (*i.e.*, diameter) of nanotubes. We mention at the outset that we employ the cylindrical coordinate system (r,ϕ,z), where the center of the SWNT under consideration is at the origin, its axis in the z direction, and r the radial distance measured from the z-axis. The interior region of the SWNT is defined as the cylindrical volume of height h and diameter d_0

$$d_0 = \frac{\sqrt{3}\sqrt{3n^2}l_{CC}}{\pi} \qquad (1)$$

which is twice the radial distance from the nanotube axis to carbon atoms. RTIL ions are considered to be in the interior of the SWNT if their center-of-mass is located inside the cylindrical volume thus defined.

MD results for the average cation and anion numbers, $N_i^{(\pm)}$, inside the SWNTs at 350 K are presented in Table 1, and the corresponding number densities are shown in Figure 1. Here and hereafter, superscripts (+) and (−) denote cations and anions, respectively. It should be noticed that there are no solvent ions present inside the (6,6) nanotube. The diameter of (6,6) is too small, and thus its tunnel is too narrow for EMI^+ and BF_4^- to enter under normal conditions (*i.e.*, ambient pressure and temperature). The size of the smallest SWNT that allows EMI^+ and BF_4^- ions inside the nanotube tunnel under normal conditions is $n = 7$ with $d_0 = 0.95$ nm. As n increases, so does the RTIL density in the interior of the SWNT.

TABLE 1. Number of Cations and Anions Inside (*n*,*n*) SWNTs[a]

n	d_0 (nm)	$N_i^{(+)}$	$N_i^{(-)}$	$\sigma_N^{(+)}$	$\sigma_N^{(-)}$
6	0.81	0	0	0	0
7	0.95	3.89	1.00	0.36	0.00
8	1.08	5.41	5.21	0.53	0.41
10	1.35	10.8	10.8	0.59	0.38
12	1.62	17.8	16.1	0.62	0.45
15	2.03	32.5	28.8	0.59	0.83
20	2.70	61.9	59.1	1.3	1.2

[a] Values of $\sigma_N^{(\pm)}$ are the standard deviations of cation and anion numbers inside the nanotubes.

Except for the $n = 7$ case, cations and anions are present in the SWNT tunnel in nearly equal amounts. We nonetheless notice that, on average, there are more cations than anions in the tunnel. Because terminal H atoms are positively charged, BF_4^- ions are attracted to the entrance regions of the tunnel (see below). However, before they can enter into the tunnel, we expect that BF_4^- ions would linger[38] in the entrance regions because (i) entry to a narrow tunnel is entropically disfavored and (ii) the Coulomb force exerted by negatively charged C atoms tends to push anions back when they attempt to enter. Cations, on the other hand, would go into the tunnel more easily than anions because of Coulomb attraction by the negatively charged C atoms. We believe that this energetic difference ("edge effect") is at least partly responsible for excess EMI^+ inside the nanotubes. Another consequence of the picture presented here is that the lingering time of ions, *viz.*, time they spend before they enter the tunnel, would increase as the d_0 decreases mainly because of (i). Therefore, it would take BF_4^- ions a long time to enter the tunnel of a small (7,7) SWNT. In this context, we caution the reader that MD statistics based on a 12 ns trajectory might not be sufficient for the $n = 7$ case because of its slow dynamics. This could explain $\sigma_N^{(-)} = 0$ we obtained for $n = 7$ (Table 1). With this caveat in mind, we investigate the solvation structure of RTIL ions inside and outside of the nanotubes.

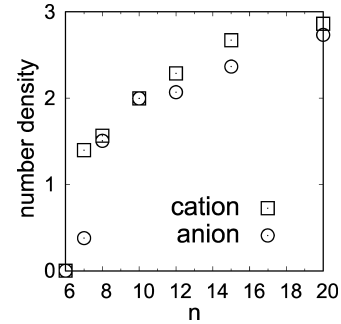

Figure 1. Number densities (nm^{-3}) of EMI^+ and BF_4^- ions in the interior of (*n*,*n*) SWNTs at 350 K. For comparison, the MD results for the cation and anion number densities in pure $EMI^+BF_4^-$ at 350 K and 1 atm are $n_0^{(\pm)} = 3.7$ nm^{-3}.

We consider distributions of EMI^+ and BF_4^- ions along the radial and axial directions. To this end, we introduce the numbers of cations and anions, $N^{(\pm)}(r,z)$, inside a cylindrical volume, which extends from $z = 0$ to $z = z$ with a base circle of radius r. $N^{(\pm)}(r,z)$ is related to local number densities $\rho^{(\pm)}(r,\phi,z)$ of cations and anions *via*

$$N^{(\pm)}(r,z) = \int_0^r \int_0^{2\pi} \int_0^z r' \mathrm{d}r' \mathrm{d}\phi' \mathrm{d}z' \rho^{(\pm)}(r',\phi',z') \quad (2)$$

where the center-of-mass is used to represent the positions of individual ions. In terms of $N^{(\pm)}(r,z)$, the average RTIL ion numbers $N_i^{(\pm)}$ in the interior of SWNTs in Table 1 are given as

$$N_i^{(\pm)} = N^{(\pm)}(d_0/2, h/2) - N^{(\pm)}(d_0/2, -h/2) \quad (3)$$

where d_0 and h are the diameter (eq 1) and length of the SWNT. We define dimensionless radial distributions of ions as

$$\xi^{(\pm)}(r) = (2\pi n_0^{(\pm)} r h)^{-1} \frac{\partial}{\partial r}[N^{(\pm)}(r, h/2) - N^{(\pm)}(r, -h/2)] \quad (4)$$

where $n_0^{(\pm)}$ denotes the cation and anion number densities in the bulk; $\xi(r)$ thus defined is characterized by an asymptotic behavior $\xi^{(\pm)}(r) \to 1$ as $r \to \infty$ just like (spherically averaged) radial distribution functions widely used in the analysis of liquid structures; $\xi^{(\pm)}(r)$ gauges variations of RTIL densities as the distance r from the nanotube axis increases.

The MD results for $\xi^{(\pm)}(r)$ are presented in Figure 2. For clear exposition of number density variations with r, the product $r\xi^{(\pm)}(r)$ of the radial distribution and the Jacobian r is displayed there. Except in the bulk region far from the nanotubes, $\xi^{(\pm)}(r)$ shows marked oscillations both inside and outside of SWNTs and DWNTs. Hereafter, RTIL distributions in these regions will be referred to as internal and external solvation structures, respectively. For convenience, we separately number the internal and external solvation shells in sequence in the order of the increasing distance from the nanotube surface. Thus, in this convention, the first external shell refers to the solvation structure outside the nanotubes, located closest to their exterior wall, while the second external shell corresponds to the next closest structure. The first internal solvation shell on the other hand refers to the inner solvation structure that is closest to the interior nanotube wall, *viz.*, the outermost shell inside of the nanotubes.

We first consider external solvation structures which show similar characteristics regardless of the nanotube diameter. To be specific, cation and anion distributions form smeared-out cylindrical shell-like structures (see Figures 2 and 4) outside of all nanotubes studied here, with a primary and a secondary peak located around 0.35 and 0.8 nm from the exterior nanotube surface, respectively. The position of the first peak of EMI^+ is slightly closer to the nanotube wall than that of BF_4^-. By contrast, the peaks of other external solvation shells of EMI^+ are situated farther from the nanotube than those of BF_4^-.

To gain insight into this trend in peak locations, we have analyzed the orientation of the imidazole ring of cations, in particular, the probability distribution $P(\theta)$ of angle θ between the normal vector to the imidazole ring and the radial direction to the midpoint of two nitrogen atoms of the ring. The results in Figure 3a show that the imidazole ring of EMI^+ in the first external solvation shell is mainly parallel to the SWNT surface. This stacking orientation allows bulky cations to approach the nanotube surface more closely than corresponding anions in the first solvation shell. By contrast, $P(\theta)$ of cations in the second external solvation shell is nearly independent of θ (Figure 3b), indicating that their ring orientation is essentially isotropic with respect to the radial direction. It should be pointed out that stacking of cations on the nanotube surface occurs despite the absence of explicit π-interactions between EMI^+ and nanotubes in our model description. Similar stacking was found between imidazole rings and benzene-like structures in prior studies.[29,30,32] We ascribe this "π-stacking" to planar geometry of the imidazole ring and nanotube honeycomb; for planar molecules subject to an external pressure, stacking minimizes the system volume and thus provides a stable configuration.

As an illustration of our results above, a snapshot of RTIL ions in the presence of a (8,8) SWNT is exhibited in Figure 4. It shows a very distinctive first external solvation shell of cylindrical symmetry with EMI^+ ions π-stacked on the exterior wall of the nanotube. We no-

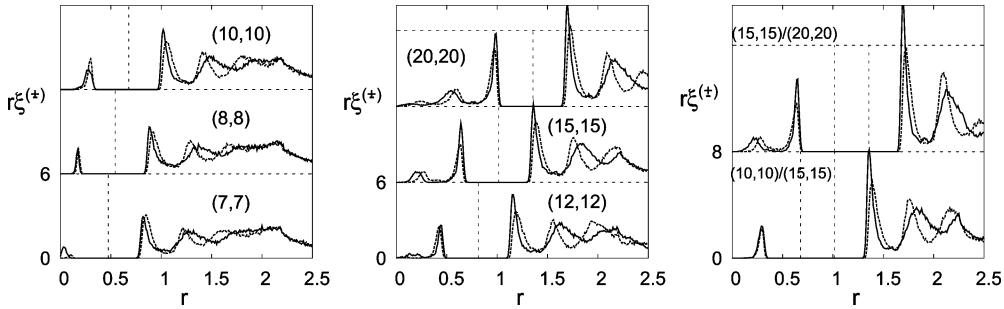

Figure 2. Radial distributions of EMI^+ (—) and BF_4^- (· · ·) inside and outside of SWNTs and DWNTs at 350 K; r is the distance (nm) from the nanotube axis, and the dashed vertical lines denote the positions of nanotube walls.

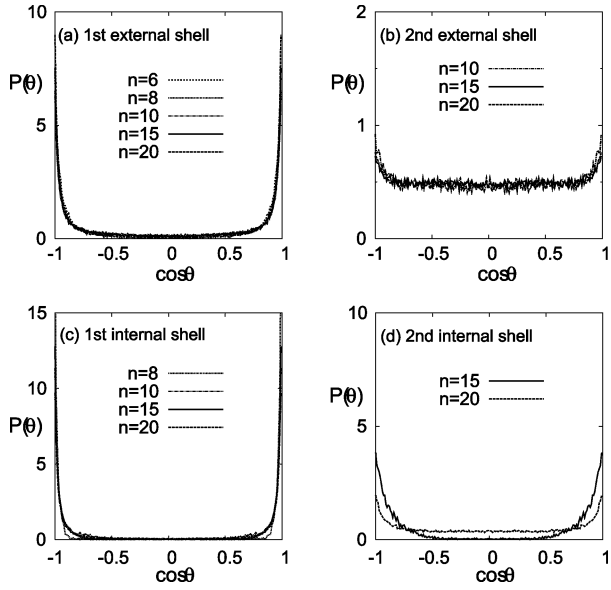

Figure 3. $P(\theta)$ for EMI^+ rings in the internal and external solvation shells of SWNTs; θ is the angle between the ring normal and the radial vector from the nanotube axis to the midpoint of two N atoms of the ring. $P(\theta)$ is normalized as $\int d(\cos\theta)P(\theta) = 1$. Both internal and external solvation shells are numbered in the order of the increasing distance from the nanotube wall.

tice that the low density region outside of the first shell is surrounded by a smeared-out but discernible second solvation shell. Ring orientations of EMI^+ ions there are very randomized compared to the first solvation shell. This suggests that $EMI^+BF_4^-$ can adjust its cation ring orientations easily to its environment; the transition from π-stacking to isotropic configurations occurs over a distance of a mere ~0.4 nm. Rapid variations of ring orientations similar to ours were also found for dimethylimidazolium cations confined inside two parallel plates.[39] We believe that this kind of flexibility in ring orientations and resulting easy adoption of π-stacking play a significant role in enabling imidazolium-based RTILs to disperse carbon nanotubes. In particular, our finding here supports the conjecture by Fukushima and Aida[21] that "imidazolium ions adsorbed on the nanotube surfaces through π interactions... trigger the clustering of the surrounding imidazolium ions in the bulk phase and interconnect neighboring SWNT bundles to form numerous physical cross-links." In this context, it would be highly desirable to extend the present study to investigate RTIL structures in the presence of multiple SWNTs. This will help to understand molecular details of, for example, cross-linking of SWNTs *via* RTIL ions.

Returning to Figure 2, we consider the internal region of nanotubes. Since SWNTs and DWNTs are characterized by very similar radial distributions of ions, we consider only the former in detail here. One of the most salient features of $\xi^{(\pm)}(r)$ in the interior of SWNTs is that the number of their peaks increases with the nanotube size. Up to $n \approx 10$ (*viz.*, $d_0 \approx 1.4$ nm), only one solvation shell exists inside the nanotubes. As n grows to $n = 12$ ($d_0 = 1.62$ nm), a second internal structure begins to appear; $\xi^{(\pm)}(r)$ for (15,15) is characterized by a distinct second internal peak at $r \approx 0.3$ nm. As n further increases to $n = 20$, the RTIL radial distributions develop a third internal shell. To avoid any confusion, we add a remark here: in view of Figure 4, some of these internal solvation "shells" may not have a cylindrical shell structure. We nonetheless refer to them as shells for simplicity.

In the case of multiple internal solvation shells (*i.e.*, $n \gtrsim 12$), the peak position of the first internal shell of the cations is a little closer to the SWNT surface than that of the anions. Analogous to the first external solvation shell, this is attributed to the stacking of the imidazole ring of EMI^+ ions on to the interior wall of nanotubes (Figure 3c). It is noteworthy in Figure 3d that the cations in the second internal shell of (15,15) show a significant degree of ordering in their ring orientation. Though not shown here, we point out that the EMI^+ rings there do not stack on those in the first internal shell, probably due to strong Coulomb repulsion. In this sense, the ring orientation in the second internal solvation shell of (15,15) is not exactly π-stacking. Rather, the available volume there is small, so that the EMI^+ rings adopt a relatively ordered configuration. $P(\theta)$ of the corresponding cations of the larger (20,20) is much more isotropic than the (15,15) case. Because of large available volume in the former, entropy plays a more prominent role in the determination of ring orientations than in the latter.

We proceed to variations of RTIL densities inside the nanotube along the axial direction. We introduce radially and azimuthally averaged RTIL densities in the interior of nanotubes

$$\zeta_i^{(\pm)}(z) = (\pi n_0^{(\pm)} d_0^2/4)^{-1} \int_0^{d_0/2} \int_0^{2\pi} r' dr' d\phi' \rho^{(\pm)}(r', \phi', z) = (\pi n_0^{(\pm)} d_0^2/2)^{-1} \frac{\partial}{\partial z} N^{(\pm)}(d_0/2, z) \quad (5)$$

which will be referred to as z distributions hereafter. Analogous to $\xi^{(\pm)}(r)$ in eq 4, $\zeta_i^{(\pm)}(z)$ is dimensionless. In Figure 5, the results for $\zeta_i^{(\pm)}(z)$ are exhibited. For comparison, z distributions of EMI^+ and BF_4^- in the first external solvation shell are also displayed. For all cases studied here, the cation-rich/anion-deficient and anion-rich/cation-deficient regions alternate in a very regular manner along the z direction in the first external solvation shell. We ascribe this feature of charge alternations to the local dipole moment arising from partially charged H and C atoms at both ends of the nanotubes. This is reminiscent of oscillations of RTIL charge density induced by a central charge found in our earlier study.[30] Except for the amplitude, the oscillatory character of the z distributions of the first external shell (*e.g.*, peak locations) varies little with the nanotube diameter. Though not presented here, DWNTs show a similar behavior.

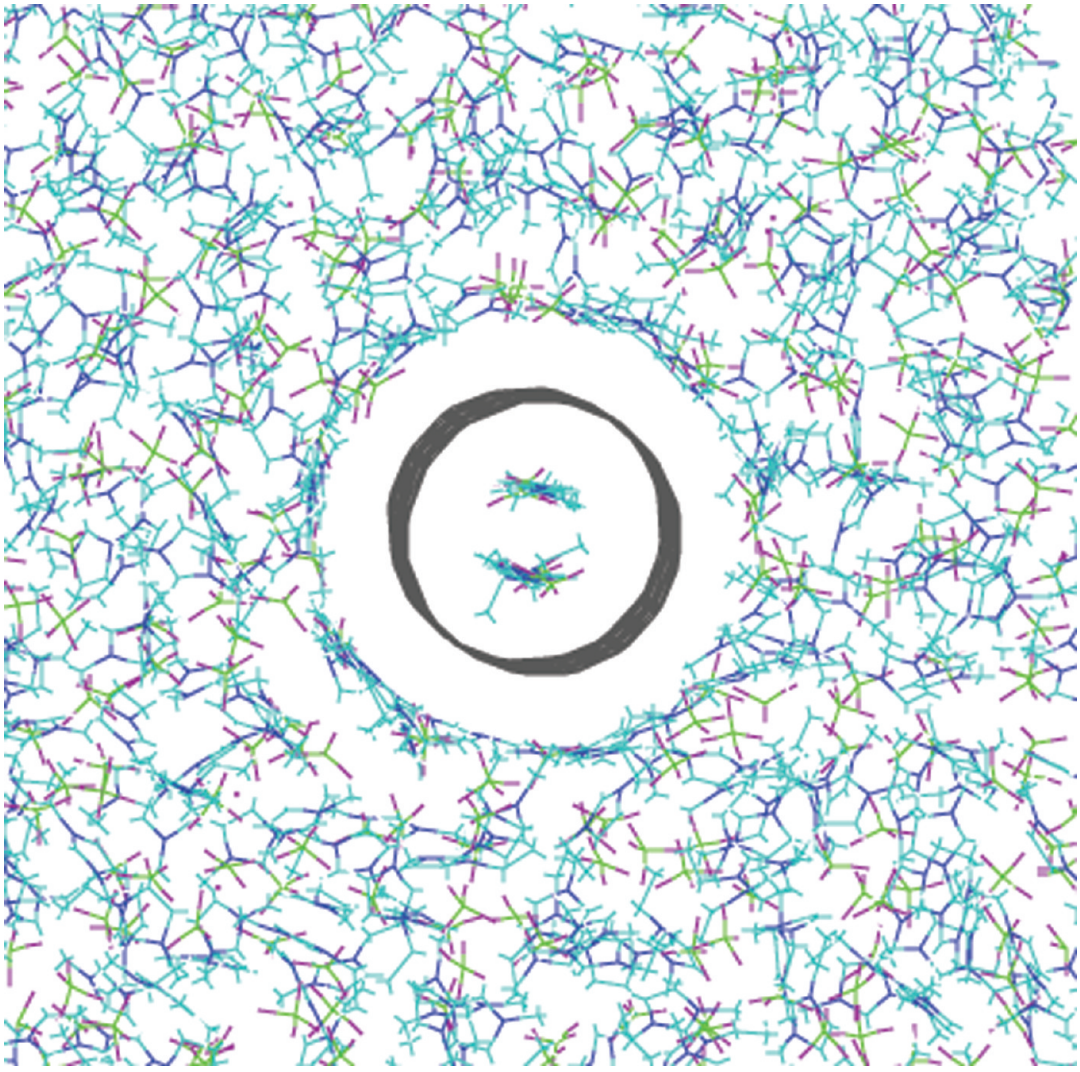

Figure 4. Snapshot of $EMI^+BF_4^-$ in the presence of a (8,8) SWNT at 350 K.

The z distributions in the interior of SWNTs vary quite dramatically with the size of the tunnel. For $n = 7$ in Figure 5a, the cations and anions are characterized by totally different z distributions; $\zeta_i^{(+)}(z)$ shows several peaks inside the nanotube, whereas there is only one peak for $\zeta_i^{(-)}(z)$. The latter also has huge peaks around $z \approx \pm 2.2$ nm, indicating significant anion populations near the tunnel entrances. While some of the aspects of $\zeta_i^{(\pm)}(z)$ in Figure 5a could be an artifact arising from slow dynamics mentioned above, they nevertheless reveal the edge effect of partially charged H and C atoms on RTIL solvation structure, especially for nanotubes of small diameter.

As we vary SWNTs from $n = 7$ to 8, the z distributions change drastically. A mere 0.14 nm increase in d_0 (Table 1) induces a dramatic transition in internal solvation structure from completely incongruent (Figure 5a) to essentially identical z distributions of EMI^+ and BF_4^- (Figure 5b)! One of the most noteworthy features of $\zeta_i^{(\pm)}(z)$ for $n = 8$ is their very regular oscillations; their amplitude and period change little along z throughout the entire nanotube tunnel. The congruent z distributions for EMI^+ and BF_4^- suggest that there is a pairing of a cation and an anion situated at locations of the same z. There are 5−6 such pairs (*cf.* Table 1) inside the (8,8) SWNT of length 3.742 nm. The $n = 10$ case in Figure 5c, on the other hand, is characterized by alternating cation and anion distributions, each with 10−11 oscillations inside the nanotube. In view of the results in Table 1, we identify each peak of $\zeta_i^{(\pm)}(z)$ there as the average location of individual EMI^+ and BF_4^- ions in the tunnel (see below).

As d_0 further grows from 1.35 nm ($n = 10$) to 1.62 nm ($n = 12$), the distributions of solvent ions become disordered. This trend can be understood in terms of the increase in available volume and thus the enhanced role of entropy in the determination of solvation structure. Comparison of panels d and e in Figure 5, however, discloses that the trend of growing disorder with d_0 does not always hold; the larger (15,15) is characterized by more orderly behavior of $\zeta_i^{(\pm)}(z)$ than the smaller (12,12). Except for a few minor structures, the alternat-

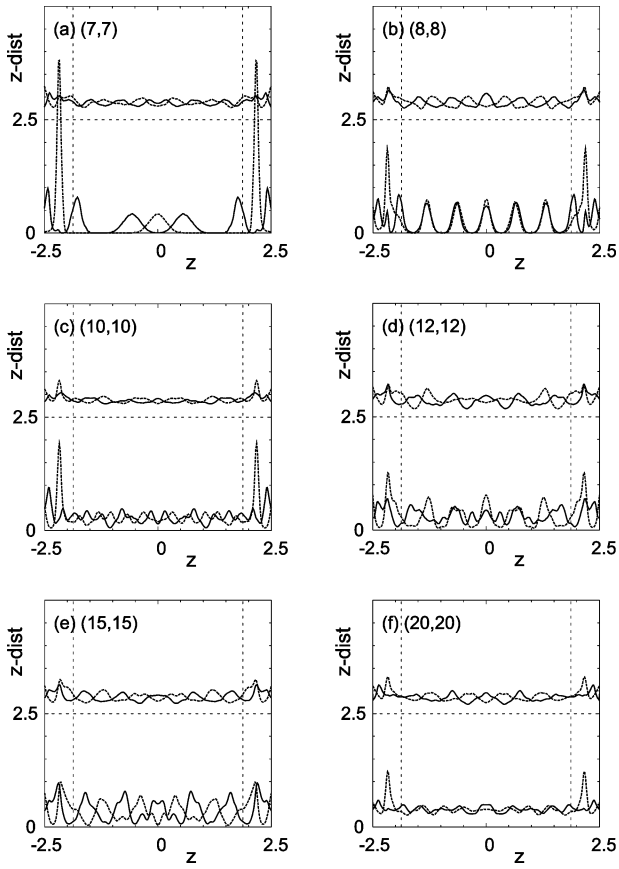

Figure 5. The *z* distributions of cations (—) and anions (· · ·) in the first external solvation shell and in the interior of SWNTs. For clarity, the *z* distributions of the first external solvation shell are shifted upward with respect to those of the nanotube interior by 2.5. The dashed vertical lines denote the positions of terminal H atoms of the nanotubes along *z* (nm).

ing cation and anion distributions in the former show very periodic oscillations of large and nearly constant amplitude. We will return to this unexpectedly "ordered" internal solvation structure of (15,15) below. The RTIL ions in the inside of (20,20) show rather homogeneous *z* distributions with minor fluctuations.

With the exception of (15,15), the *z* distribution of BF_4^- in the entrance regions of the tunnel around $z = \pm 2.2$ nm is considerably higher than that of EMI^+. As mentioned above, this result is attributed to the edge effect, *viz.*, Coulomb forces arising from partially charged H and C atoms, which favor entrance of cations into the nanotube tunnel. The peak height of $\zeta_i^{(-)}(z)$ in the entrance regions generally decreases with growing *n*, indicating an increasingly more important role of entropy.

To gain better understanding of pronounced changes of internal solvation structure with the SWNT diameter, we examine relative orientations of individual RTIL ions in the first solvation shell inside the nanotube tunnels. Before we embark on our analysis, we take a brief look at snapshots of EMI^+ and BF_4^- ions in the interior of nanotubes. Figure 6 exposes striking changes of the first internal solvation shell structure with d_0. For (7,7), which is the smallest nanotube that allows RTIL ions inside the tunnel, we have a single file distribution of ions. This changes to a zigzag distribution of cations and similarly for anions inside of (8,8). For additional insight, the same snapshot configurations inside the $n = 7$ and 8 SWNTs are displayed in Figure 7 in the space-filling representation of RTIL ions. We notice that there is empty space between imidazolium ions inside (7,7) arising from their direct Coulomb repulsion. This explains its low internal ion density, compared to the $n = 8$ case (*cf.* Figure 1).

Returning to Figure 6, we notice that the solvation structure in the interior of (10,10) is characterized by helical distributions of RTIL ions, while it becomes rather disordered inside (12,12). As noted above, (15,15) shows ordered internal solvation structure. Specifically, the cation and anion distributions in its first internal solvation shell separately develop pentagonal structures, which are in a staggered configuration. Figure 6f shows a mostly disordered first internal solvation shell for (20,20). Nevertheless, EMI^+ and BF_4^- ions there appear to form a weak octagonal structure.

To obtain a quantitative picture for EMI^+ and BF_4^- distributions inside nanotubes and to check if the snapshots in Figure 6 properly depict ensemble-averaged solvation structures, we proceed as follows: We first order ions of our interest by their position, in particular, in the descending order of their *z* coordinate values. Thus, positions (r_i,ϕ_i,z_i) of the ordered group of ions satisfy $z_1 > z_2 > z_3 > \ldots$, where *i* labels the ions. We define the rotational angle between two neighboring ions *i* and $i + 1$ as

$$\psi_i \equiv \phi_{i+1} - \phi_i \quad (-180^\circ < \psi_i < 180^\circ) \tag{6}$$

Thus if we rotate the radial vector of *i* by ψ_i, it will be in the direction of that of $i + 1$. If the sign of ψ_i does not change for the group of ions under consideration, their distribution is, in general, chiral. In this case, positive (negative) ψ_i corresponds to counterclockwise (clockwise) progression. If $\psi_i \approx \pm 180°$, the resulting ion distribution has a zigzag structure.

We have calculated ψ_i values for cations and anions in the first internal solvation shell of SWNTs by using 100 configurations, each sampled every 100 ps from the first 10 ns of MD trajectories. The results are shown in Figure 8. For $n = 8$, $|\psi_i| \approx 180°$ for both EMI^+ and BF_4^- ions. This confirms that cations and anions separately form zigzag distributions inside the (8,8) nanotube tunnel. Near perfect pairing of EMI^+ and BF_4^- ions mentioned above is also confirmed by the excellent agreement of their *z* values.

The majority of cations and anions in Figure 8b are characterized by $\psi_i \approx 130°$, revealing the helical nature of their distributions inside of (10,10). Furthermore, the positive sign of ψ_i for both the cations and anions shows that their distributions have the same chirality, *viz.*, counterclockwise progression. For additional insight,

we have analyzed rotational angles by treating cations and anions as a *single* group rather than separating them into two different groups by species. With a few exceptions, we obtained $\psi_i \approx -120°$ (Figure 8c). This means that EMI^+ and BF_4^- ions together also form a helical distribution, but its chirality is the opposite of that of respective cation and anion distributions. This structure is possible only if the individual cations and anions alternate in the z direction (*cf.* Figure 5c), and each intervening, say, cation occupies the interior wall opposite from its two neighboring anions. We consider an example for illustration. Suppose two neighboring anions at z_i and z_{i+1} occupy, for instance, the 12 o'clock and 8 o'clock positions inside the nanotube, respectively, when we look through its tunnel. Then the orientation of the intervening cation situated between z_i and z_{i+1} is in the 4 o'clock direction. For comparison, the ψ_i results for the (10,10)/(15,15) DWNT are displayed in Figure 8d. Though considerably disordered compared to the (10,10) case, its EMI^+ and BF_4^- distributions also show a non-negligible degree of chirality.

We should mention that we have not found chiral distributions with $\psi_i < 0$, *viz.*, clockwise progression, inside of (10,10); that is, our simulations yielded only the counterclockwise progression with $\psi_i > 0$ (Figure 8b). This suggests that chiral distributions of EMI^+ and BF_4^- inside of (10,10) are very stable, and as a result, transitions between distributions of differing chirality, $\psi_i > 0$ and $\psi_i < 0$, occur slowly, probably on a time scale considerably longer than 12 ns employed for production runs in our simulations.

The scattered ψ_i plot in Figure 8e indicates disordered distributions of ions inside the (12,12) SWNT. By contrast, Figure 8f presents clear evidence of well-ordered first internal solvation shell structure for (15,15). Specifically, the concentration of the distributions at $\psi_i \approx \pm 70$ and $\pm 140°$ demonstrates that, on average, the cation and anion solvation structures have a five-fold rotational symmetry. We speculate that these pentagonal structures result because they are a perfect fit inside the (15,15) nanotube tunnel. In this context, the relative size of ions compared to the pore is among the key factors that determine internal solvation structures. Cations and anions also alternate along z in a very regular fashion, as expected from Figure 5e. Furthermore, their respective z values do not vary with ψ_i. This indicates that the first internal solvation shell of (15,15) consists of alternating layers of cations and anions along the nanotube axis. As in Figure 8c, we also analyzed ψ_i for the first internal solvation shell of (15,15) by treating all ions there as a single group. The results are exhibited in Figure 8g. We notice that in addition to $|\psi_i| \approx 70$ and 140° (Figure 8f) the distribution of rotational angles shows a significant population around $|\psi_i| = 35$, 110, and 180°. These ψ_i values indicate that orientations of ions in the first internal solvation altogether have an approximate 10-fold symmetry. Since cations and anions form pentagonal structures, we conclude that their structures are in a staggered configuration.

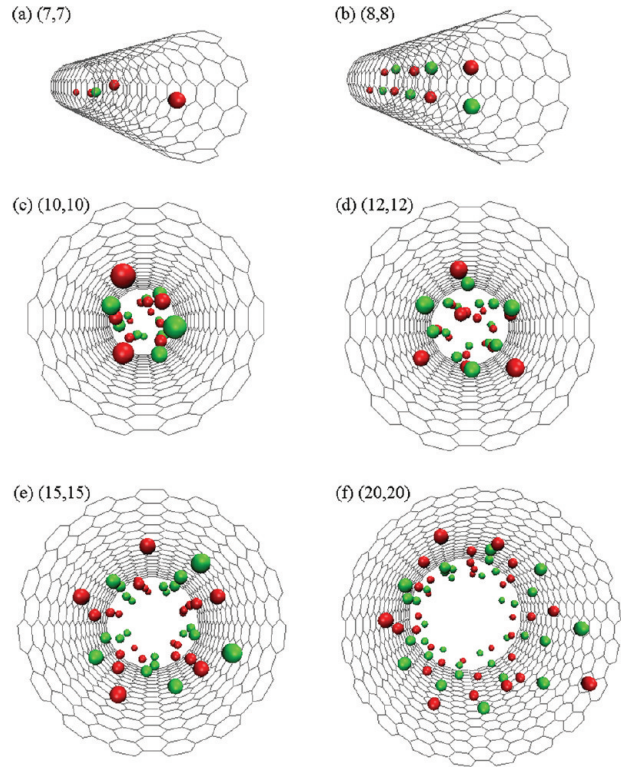

Figure 6. Snapshots of RTIL ions in the first internal solvation shell of SWNTs. Red and green balls represent locations of center-of-mass of EMI^+ and BF_4^-, respectively.

The results for (20,20) in Figure 8h show that the distributions of EMI^+ and BF_4^- in the first internal solvation shell are characterized by significant probabilities at $|\psi_i| \approx 45$, 90, 135, and 180°. This indicates that, though disordered, the cations and anions separately form octagonal structures on average.

Our analysis of ψ_i summarized in Figure 8 confirms that most of the observations we made for Figure 6 above are valid for solvation structures of (n,n) nanotubes. This indicates that the snapshot configurations there indeed provide good representations of the ensemble-averaged first internal solvation shell structures. It also implies relatively high stability of ordered solvation structures in that their main characteristics are maintained during the MD simulations.

CONCLUDING REMARKS

In this article, we have studied solvation of single-walled and double-walled carbon nanotubes in the

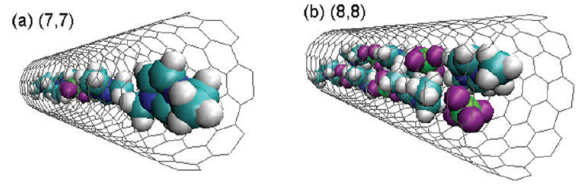

Figure 7. Internal solvation configurations of Figure 6a,b in the space-filling representation of RTIL ions.

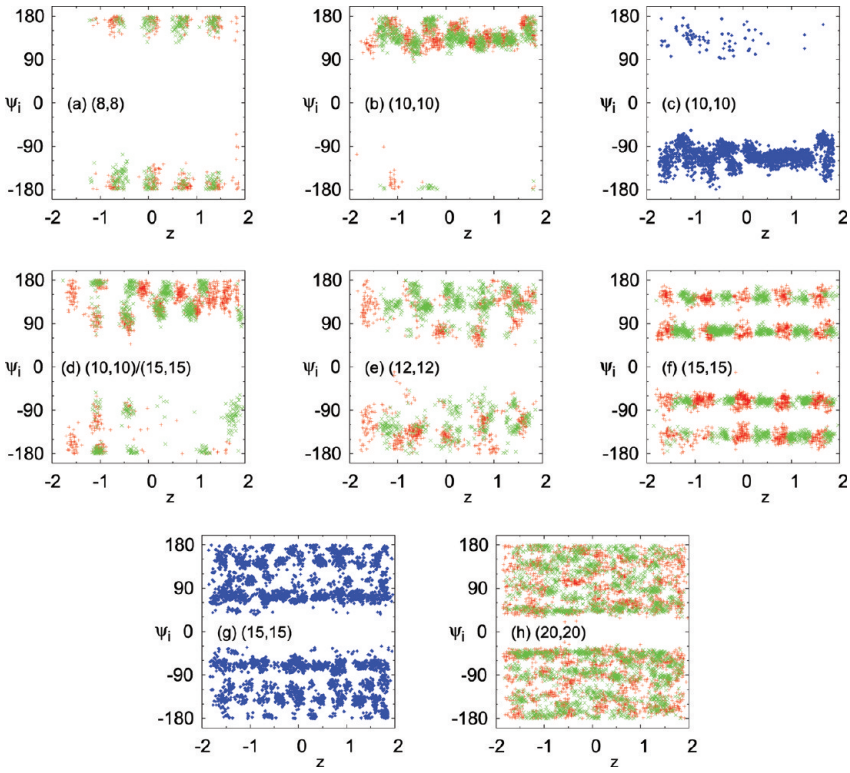

Figure 8. Rotational angle ψ_i for EMI^+ and BF_4^- ions in the first internal solvation shell of nanotubes. Red and green markers represent the results for the cations and anions, respectively, while those in blue are obtained by treating both species as a single group.

armchair configuration in $EMI^+BF_4^-$ using MD simulations. We have found that solvent cations and anions form smeared-out cylindrical shell structures outside of the nanotubes. For all cases we studied, *viz.*, (6,6) (7,7), (8,8), (10,10), (12,12), (15,15), and (20,20) SWNTs and (10,10)/(15,15) and (15,15)/(20,20) DWNTs, the imidazole ring of EMI^+ ions in the first external solvation shell tends to π-stack on the exterior nanotube wall. By contrast, cations in the second external solvation shell show nearly isotropic ring orientations with respect to the radial direction. We conjecture that this kind of good adaptability of ring orientations to differing environments is one of the important factors contributing to imidazolium-based RTILs' good capability of dispersing carbon nanotubes.

We found that RTIL distributions in the interior of nanotubes vary rather dramatically with the nanotube diameter. To be specific, solvation structures of EMI^+ and BF_4^- inside of (*n*,*n*) SWNTs are characterized by a single file distribution of cations and anions ($n = 7$ and $d_0 = 0.95$ nm), zigzag distributions with ion pairing ($n = 8$ and $d_0 = 1.08$ nm), chiral distributions ($n = 10$ and $d_0 = 1.35$ nm), disordered structure ($n = 12$ and $d_0 = 1.62$ nm), staggered pentagonal first solvation shell structures with alternating layers of cations and anions ($n = 15$ and $d_0 = 2.03$ nm), and disordered octagonal structures in a staggered configuration ($n = 20$ and $d_0 = 2.70$ nm). EMI^+ and BF_4^- ions do not enter into the (6,6) nanotube tunnel spontaneously under normal conditions.

The formation of ordered structures inside nanotubes has been known for some time. For example, water molecules confined in the nanotube tunnel develop different solvation structures, such as helical and hexagonal distributions, depending on the nanotube size and thermodynamic conditions (and potential models employed), according to several prior simulation studies.[40−46] The structure and optoelectronic properties of crystallites of simple ionic systems such as KI and CsI inside nanotubes were also studied.[47−50] Our analysis here shows that, despite bulky ion size and complete lack of symmetry for cations, $EMI^+BF_4^-$ shows rich solvation structures of ordered and disordered nature inside nanotubes, and small modulations of d_0 induce major changes in the internal solvation structures. This finding clearly exposes that nanoscale confinement exerts a far-reaching influence on RTIL ion distributions inside a pore. In addition to electrostatic interactions which we believe are mainly responsible for various patterns of cation and anion alternations, relative size, and shape of ions compared to the pore seem to play a central role in the determination of ordered and disordered internal solvation structures and their stability. We thus think that the anomalous behavior of specific capacitance with the pore size[51,52] found recently for micropores of size $\lesssim$1 nm is directly related to the startling changes of solvation structure of $EMI^+BF_4^-$ inside small nanotubes with their diameter. Also, the formation of various ordered structures of RTIL ions with high stability we found inside nanotubes seems to be in excellent accord with recent X-ray diffraction and differential scanning calorimetry measurements.[28]

It would be worthwhile in the future to extend the present study in several different directions. First, it would be interesting to investigate how the confinement affects dynamic properties of RTILs, such as dynamic heterogeneity.[53] Along this avenue, we are currently analyzing transport properties of RTIL ions inside nanotubes. Second, it would be worthwhile to study the influence of internal solvation on electronic properties of nanotubes and its variations with the nanotube diameter. Another very important extension would be a detailed analysis of external solvation of multiple nanotubes. As mentioned above, this will help to understand the RTILs' good capability of dispersing nanotubes and thus clarify its gelation mechanism at the molecular level. Finally, improvement of the potential

model for nanotubes with account of, for example, polarizability and π-electron density would be desirable. According to previous simulation studies in normal[54−56] and RTIL[57] solvents, the solute polarizability can exert a non-negligible influence on solvation structure and dynamics. To be specific, while it tends to decelerate solute and solvent dynamics,[54−57] both enhancement and reduction of solvent structures around polarizable solutes, compared to nonpolarizable solutes, have been observed.[55,57] We thus expect that the inclusion of nanotube polarizability would, for example, enhance solvation structures very close to the nanotube walls but soften other structures and reduce the edge effect. Therefore, while qualitative features of our present study would remain largely valid, a systematic analysis of polarizability effects would be very helpful to quantitative understanding of solvation of nanotubes in both normal solvents and ionic liquids.

SIMULATION METHODS

The simulation cell comprised either a (*n*,*n*) single-walled or a (*n*,*n*)/(*m*,*m*) double-walled carbon nanotube immersed in $EMI^+BF_4^-$. Seven different SWNTs, $n = 6$, 7, 8, 10, 12, 15, and 20, and two different DWNTs, (10,10)/(15,15) and (15,15)/(20,20), were examined. We employed 400 pairs of EMI^+ and BF_4^- to solvate the (20,20) SWNT and (15,15)/(20,20) DWNT. For all other cases, 344 pairs were used.

The MD simulations were performed using the DL_POLY program.[58] To determine the densities of nanotube−RTIL systems, we first conducted simulations in the NPT ensemble at 350 K and 1 atm for 6 ns after annealing from 1000 K. RTIL ions were allowed to move in and out of the nanotube tunnel during the simulations. Using the density thus obtained, we then simulated molecular dynamics in the canonical ensemble at 350 K. The long-range electrostatic interactions were computed *via* the Ewald method, resulting in essentially no truncation of these interactions. The trajectories were integrated *via* the Verlet leap-frog algorithm using a time step of 2 fs. Simulations in the canonical ensemble were carried out with 4 ns equilibration, followed by a 12 ns trajectory from which averages were computed.

Acknowledgment. This research was supported in part by the National Science Foundation through TeraGrid resources provided by Pittsburgh Supercomputing Center.

REFERENCES AND NOTES

1. For recent reviews, see: Welton, T. Ionic Liquids in Catalysis. *Coord. Chem. Rev.* **2004**, *248*, 2459–2477.
2. Zhang, Z. C. Catalysis in Ionic Liquids. *Adv. Catal.* **2006**, *49*, 153–237.
3. Dupont, J.; Suarez, P. A. Z. Physico-chemical Processes in Imidazolium Ionic Liquids. *Phys. Chem. Chem. Phys.* **2006**, *8*, 2441–2452.
4. Welton, T. Room-Temperature Ionic Liquids−Solvents for Synthesis and Catalysis. *Chem. Rev.* **1999**, *99*, 2071–2084.
5. Jessop, P. G.; Eckert, C. A.; Liotta, C. L.; Bonilla, R. J.; Brown, J. S.; Brown, R. A.; Pollet, P.; Thomas, C. A.; Wheeler, C.; Wynne, D. Catalysis Using Supercritical or Subcritical Inert Gases under Split-Phase Conditions. In *Clean Solvents*; Moens, L.; Abraham, M. A., Eds.; ACS Symposium Series 819, American Chemical Society: Washington, DC 2002; pp 97−112.
6. Chiappe, C.; Pieraccini, D. Ionic Liquids: Solvent Properties and Organic Reactivity. *J. Phys. Org. Chem.* **2005**, *18*, 275–297.
7. Cull, S. G.; Holbrey, J. D.; Vargas-Mora, V.; Seddon, K. R.; Lye, G. J. Room Temperature Ionic Liquids as Replacements for Organic Solvents in Multiphase Bioprocess Operations. *Biotechnol. Bioeng.* **2000**, *69*, 227–233.
8. Huang, C.; Chen, B.; Zhang, J.; Liu, Z.; Li, Y. Desulfurization of Gasoline by Extraction with New Ionic Liquids. *Energy Fuels* **2004**, *18*, 1862–1864.
9. Jiang, Y.; Xia, H.; Guo, C.; Mahmood, I.; Liu, H. Phenomena and Mechanism for Separation and Recovery of Penicillin in Ionic Liquids Aqueous Solution. *Ind. Eng. Chem. Res.* **2007**, *46*, 6303–6312.
10. Kulkarni, P. S.; Branco, L. C.; Crespo, J. G.; Afonso, C. A. M. Capture of Dioxins by Ionic Liquids. *Environ. Sci. Technol.* **2008**, *42*, 2570–2574.
11. van Rantwijk, F.; Sheldon, R. A. Biocatalysis in Ionic Liquids. *Chem. Rev.* **2007**, *107*, 2757–2785.
12. Wildeman, S. M. A. D.; Sonke, T.; Schoemaker, H. E.; May, O. Biocatalytic Reductions: From Lab Curiosity to First Choice. *Acc. Chem. Res.* **2007**, *40*, 1260–1266.
13. Bansal, D.; Cassel, F.; Croce, F.; Hendrickson, M.; Plichta, E.; Salomon, M. Conductivities and Transport Properties of Gelled Electrolytes with and without an Ionic Liquid for Li and Li-Ion Batteries. *J. Phys. Chem. B* **2005**, *109*, 4492–4496.
14. Lee, S.-Y.; Yong, H. H.; Lee, Y. J.; Kim, S. K.; Ahn, S. Two-Cation Competition in Ionic-Liquid-Modified Electrolytes for Lithium Ion Batteries. *J. Phys. Chem. B* **2005**, *109*, 13663–13667.
15. Souza, R. F. D.; Padilha, J. C.; Gonçalves, R. S.; Dupont, J. Room Temperature Dialkylimidazolium Ionic Liquid-Based Fuel Cells. *Electrochem. Commun.* **2005**, *5*, 728–731.
16. Belieres, J.-P.; Gervasio, D.; Angell, C. A. Binary Inorganic Salt Mixtures as High Conductivity Electrolytes for >100° C Fuel Cells. *Chem. Commun.* **2006**, 4799–4801.
17. Papageorgiou, N.; Athanassov, Y.; Armand, M.; Bonhôte, P.; Pettersson, H.; Azam, A.; Grätzel, M. The Performance and Stability of Ambient Temperature Molten Salts for Solar Cell Applications. *J. Electrochem. Soc.* **1996**, *143*, 3099–3108.
18. Matsumoto, H.; Matsuda, T.; Tsuda, T.; Hagiwara, R.; Ito, Y.; Miyazaki, Y. The Application of Room Temperature Molten Salt with Low Viscosity to the Electrolyte for Dye-Sensitized Solar Cell. *Chem. Lett.* **2001**, *30*, 26–27.
19. Wang, P.; Zakeeruddin, S. M.; Moser, J.-E.; Humphry-Baker, R.; Grätzel, M. A Solvent-Free, $SeCN^-/(SeCN)_3^-$ Based Ionic Liquid Electrolyte for High-Efficiency Dye-Sensitized Nanocrystalline Solar Cells. *J. Am. Chem. Soc.* **2004**, *126*, 7164–7165.
20. Fukushima, T.; Kosaka, A.; Ishimura, Y.; Yamamoto, T.; Takigawa, T.; Ishii, N.; Aida, T. Molecular Ordering of Organic Molten Salts Triggered by Single-Walled Carbon Nanotubes. *Science* **2003**, *300*, 2072–2074.
21. Fukushima, T.; Aida, T. Ionic Liquids for Soft Functional Materials with Carbon Nanotubes. *Chem.—Eur. J.* **2007**, *13*, 5048–5058.
22. Zhao, F.; Wu, X.; Wang, M.; Liu, Y.; Gao, L.; Dong, S. Electrochemical and Bioelectrochemistry Properties of Room-Temperature Ionic Liquids and Carbon Composite Materials. *Anal. Chem.* **2004**, *76*, 4960–4967.
23. Katakabe, T.; Kaneko, T.; Watanabe, M.; Fukushima, T.; Aida, T. Electric Double-Layer Capacitors Using Bucky Gels Consisting of an Ionic Liquid and Carbon Nanotubes. *J. Electrochem. Soc.* **2005**, *152*, A1913–A1916.
24. Maleki, N.; Safavi, A.; Tajabadi, F. High-Performance Carbon Composite Electrode Based on an Ionic Liquid as a Binder. *Anal. Chem.* **2006**, *78*, 3820–3826.
25. Kachoosangi, R. T.; Wildgoose, G. G.; Compton, R. G. Room Temperature Ionic Liquid Carbon Nanotube Paste Electrodes: Overcoming Large Capacitive Currents Using Rotating Disk Electrodes. *Electroanalysis* **2007**, *19*, 1483–1489.

26. Kachoosangi, R. T.; Musameh, M. M.; Abu-Yousef, I.; Yousef, J. M.; Kanan, S. M.; Xiao, L.; Davies, S. G.; Russell, A.; Compton, R. G. Carbon Nanotube-Ionic Liquid Composite Sensors and Biosensors. *Anal. Chem.* **2009**, *81*, 435–442.
27. Yu, P.; Yan, J.; Zhao, H.; Su, L.; Zhang, J.; Mao, L. Rational Functionalization of Carbon Nanotube/Ionic Liquid Bucky Gel with Dual Tailor-Made Electrocatalysts for Four-Electron Reduction of Oxygen. *J. Phys. Chem. C* **2008**, *112*, 2177–2182.
28. Chen, S.; Wu, G.; Sha, M.; Huang, S. Transition of Ionic Liquid [bmim][PF6] from Liquid to High-Melting-Point Crystal When Confined in Multiwalled Carbon Nanotubes. *J. Am. Chem. Soc.* **2007**, *129*, 2416–2417.
29. Hanke, C. G.; Johansson, A.; Harper, J. B.; Lynden-Bell, R. M. Why are Aromatic Compounds more Soluble than Aliphatic Compounds in Dimethylimidazolium Ionic Liquids? A Simulation Study. *Chem. Phys. Lett.* **2003**, *374*, 85–90.
30. Shim, Y.; Choi, M. Y.; Kim, H. J. A Molecular Dynamics Computer Simulation Study of Room-Temperature Ionic Liquids: I. Equilibrium Solvation Structure and Free Energetics. *J. Chem. Phys.* **2005**, *122*, 044510/12.
31. Shim, Y.; Choi, M. Y.; Kim, H. J. A Molecular Dynamics Computer Simulation Study of Room-Temperature Ionic Liquids: II. Equilibrium and Nonequilibrium Solvation Dynamics. *J. Chem. Phys.* **2005**, *122*, 044511/12.
32. Maolin, S.; Fuchun, Z.; Guozhong, W.; Haiping, F.; Chunlei, W.; Shimou, C.; Yi, Z.; Jun, H. Ordering Layers of [bmim][PF6] Ionic Liquid on Graphite Surfaces: Molecular Dynamics Simulation. *J. Chem. Phys.* **2008**, *128*, 134504/7.
33. Lu, D.; Li, Y.; Ravaioli, U.; Schulten, K. Empirical Nanotubes Model for Biological Applications. *J. Phys. Chem. B* **2005**, *109*, 11461–11467.
34. Hummer, G.; Rasaiah, J. C.; Noworyta, J. P. Water Conduction through the Hydrophobic Channel of a Carbon Nanotube. *Nature* **2001**, *414*, 188–190.
35. Canongia Lopes, J. N. Modeling Ionic Liquids Using a Systematic All-Atom Force Field. *J. Phys. Chem. B* **2004**, *108*, 2038–2047.
36. Canongia Lopes, J. N.; Deschamps, J.; Padua, A. A. H. Modeling Ionic Liquids Using a Systematic All-Atom Force Field. *J. Phys. Chem. B* **2004**, *108*, 11250.
37. Jeroen, W. G. W.; Liesbeth, C. V.; Andrew, G. R.; Richard, E. S.; Cees, D. Atomic Structure and Electronic Properties of Single-Walled Carbon Nanotubes. *Nature* **1998**, *391*, 62–64.
38. Sint, K.; Wang, B.; Král, P. Selective Ion Passage through Functionalized Graphene Nanopores. *J. Am. Chem. Soc.* **2008**, *130*, 16448–16449.
39. Pinilla, C.; Del Pópolo, M. G.; Lynden-Bell, R. M.; Kohanoff, J. Structure and Dynamics of a Confined Ionic Liquid. Topics of Relevance to Dye-Sensitized Solar Cells. *J. Phys. Chem. B* **2005**, *109*, 17922–17927.
40. Mao, Z.; Sinnott, S. B. A Computational Study of Molecular Diffusion and Dynamic Flow through Carbon Nanotubes. *J. Phys. Chem. B* **2000**, *104*, 4618–4624.
41. Mashl, R. J.; Joseph, S.; Alura, N. R.; Jakobsson, E. Anomalously Immobilized Water: A New Water Phase Induced by Confinement in Nanotubes. *Nano Lett.* **2003**, *3*, 589–592.
42. Lee, K. H.; Sinnott, S. B. Computational Studies of Non-Equilibrium Molecular Transport through Carbon Nanotubes. *J. Phys. Chem. B* **2004**, *108*, 9861–9870.
43. Liu, Y.; Wang, Q.; Wu, T.; Zhang, L. Fluid Structure and Transport Properties of Water inside Carbon Nanotubes. *J. Chem. Phys.* **2005**, *123*, 234701/7.
44. Liu, Y.; Wang, Q. Transport Behavior of Water Confined in Carbon Nanotubes. *Phys. Rev. B* **2005**, *72*, 085420/4.
45. Barros, E. B.; Jorio, A.; Samsonidze, G. G.; Capaz, R. B.; Souza, A. G.; Mendes, F. J.; Dresselhaus, G.; Dresselhaus, M. S. Review on the Symmetry-Related Properties of Carbon Nanotubes. *Phys. Rep.* **2006**, *431*, 261–302.
46. Alexiadis, A.; Kassinos, S. Molecular Simulation of Water in Carbon Nanotubes. *Chem. Rev.* **2008**, *108*, 5014–5034.
47. Wilson, M.; Madden, P. A. Growth of Ionic Crystals in Carbon Nanotubes. *J. Am. Chem. Soc.* **2001**, *123*, 2101–2102.
48. Wilson, M. The Formation of Low-Dimensional Ionic Crystallites in Carbon Nanotubes. *J. Chem. Phys.* **2002**, *116*, 3027–3041.
49. Yam, C.; Ma, C.; Wang, X.; Chen, G. Electronic Structure and Charge Distribution of Potassium-Iodide-Intercalated Single-Walled Carbon Nanotubes. *Appl. Phys. Lett.* **2004**, *85*, 4484–4486.
50. Bichoutskaia, E.; Pyper, N. C. Theoretical Study of the Structures and Electronic Properties of All-Surface KI and CsI Nanocrystals Encapsulated in Single Walled Carbon Nanotubes. *J. Chem. Phys.* **2008**, *129*, 154701/15.
51. Chmiola, J.; Yushin, G.; Gogotsi, Y.; Portet, C.; Simon, P.; Taberna, P. L. Anomalous Increase in Carbon Capacitance at Pore Sizes less than 1 Nanometer. *Science* **2006**, *313*, 1760–1763.
52. Largeot, C.; Portet, C.; Chmiola, J.; Taberna, P. L.; Gogotsi, Y.; Simon, P. Relation between the Ion Size and Pore Size for an Electric Double Layer Capacitor. *J. Am. Chem. Soc.* **2008**, *130*, 2730–2731.
53. See: Shim, Y.; Kim, H. J. On Dielectric Relaxation, Ion Conductivity, Solvent Rotation and Solvation Dynamics in a Room-Temperature Ionic Liquid. *J. Phys. Chem. B* **2008**, *112*, 11028–11038.
54. Bursulaya, B. D.; Zichi, D. A.; Kim, H. J. Role of Solute Electronic Polarizability in Solvation Dynamics. *J. Phys. Chem.* **1995**, *99*, 10069–10074.
55. Bursulaya, B. D.; Zichi, D. A.; Kim, H. J. A Molecular Dynamics Simulation Study of Polarizable Solute Solvation in Water: I. Equilibrium Solvent Structure and Solute Rotational Dynamics. *J. Phys. Chem.* **1996**, *100*, 1392–1405.
56. Bursulaya, B. D.; Kim, H. J. Effects of Solute Electronic Structure Variation on Photon Echo Spectroscopy. *J. Phys. Chem.* **1996**, *100*, 16451–16456.
57. Jeong, D.; Shim, Y.; Choi, M. Y.; Kim, H. J. Effects of Solute Electronic Polarizability on Solvation in a Room-Temperature Ionic Liquid. *J. Phys. Chem. B* **2007**, *111*, 4920–4925.
58. Forester, T. R.; Smith, W. *DL_POLY user manual*, CCLRC; Daresbury Laboratory: Warrington, U.K., 2001.